

Residual resampling-based physics-informed neural network for neutron diffusion equations*

Heng Zhang,¹ Yun-Ling He,¹ Dong Liu,^{2,3,†} Qin Hang,¹ He-Min Yao,¹ and Di Xiang^{2,3}

¹Chongqing University of Posts and Telecommunications, Chongqing 400065, China

²Science and Technology on Reactor System Design Technology Laboratory,
Nuclear Power Institute of China, Chengdu, 610213, China

³CNNC Engineering Research Center of Nuclear Energy Software and Digital Reactor, Chengdu, 610213, China

The neutron diffusion equation plays a pivotal role in the analysis of nuclear reactors. Nevertheless, employing the Physics-Informed Neural Network (PINN) method for its solution entails certain limitations. Traditional PINN approaches often utilize fully connected network (FCN) architecture, which is susceptible to overfitting, training instability, and gradient vanishing issues as the network depth increases. These challenges result in accuracy bottlenecks in the solution. In response to these issues, the Residual-based Resample Physics-Informed Neural Network (R²-PINN) is proposed, which proposes an improved PINN architecture that replaces the FCN with a Convolutional Neural Network with a shortcut (S-CNN), incorporating skip connections to facilitate gradient propagation between network layers. Additionally, the incorporation of the Residual Adaptive Resampling (RAR) mechanism dynamically increases sampling points, enhancing the spatial representation capabilities and overall predictive accuracy of the model. The experimental results illustrate that our approach significantly improves the model's convergence capability, achieving high-precision predictions of physical fields. In comparison to traditional FCN-based PINN methods, R²-PINN effectively overcomes the limitations inherent in current methods, providing more accurate and robust solutions for neutron diffusion equations.

Keywords: Neutron diffusion equation, Physics-Informed Neural Network, CNN with shortcut, Residual Adaptive Resampling

I. INTRODUCTION

Nuclear reactor core analysis is crucial for ensuring safe operation of nuclear reactors. The neutron diffusion equation, which describes neutron movement within a medium, is fundamental to this analysis[1]. Numerical methods are widely applied in many physical scenarios. Methods such as finite difference [2] and finite element [3] have been continuously developed and improved. In the reactor domain, many related works can be found. For example, Yasser Mohamed Hamada[4] proposed higher-order compact finite difference schemes for solving neutron diffusion equations. At the same time, Yuk[5] utilized the finite element method to solve the time-dependent neutron diffusion equation. X Li[6] designs an algorithm based on the finite volume method to solve multigroup neutron diffusion equations. For the same problem, Matheus Gulate Tavares[7] and K Zhuang[8] use the Source Iterative Method and variational nodal method to solve, respectively. Additionally, lots of researchers have successfully employed CFD software such as COMSOL[9], ANSYS FLUENT[10] and OpenFOAM[11] to tackle neutron diffusion problems.

However, these methods require the discretization of the

solution domain, which can be computationally complex and time-consuming when high-precision physics reconstruction is required[12]—also, considering the complex environment in nuclear reactors, which exist in multi-physics fields such as neutron transport and heat transfer. Numerical methods have to simplify and approximate the model in solving the equations, which will introduce a certain amount of solution error. Meanwhile, benefiting from the development of neural networks (NN), there has been increasing interest in machine learning-based approaches[13]. Training NN makes it possible to predict the physical field faster than traditional numerical methods. Then, engineering prior knowledge should be incorporated into the network to make NN predictions more consistent with physical laws. PINNs, introduced by Raissi[14], incorporate partial differential equations (PDEs) as constraints during network training by increasing penalties for violating PDE data points. This leads to higher precision and physically consistent solutions. Until now, PINNs have been successfully applied to various scientific computation problems in engineering fields such as fluids[15, 16], heat transfer[17, 18], flows[19, 20], and solid mechanics [21, 22], yielding significant results. The difference between PINNs and traditional numerical methods are shown in Table 1. In nuclear reactor core analysis, the Monte-Carlo method[23, 24] and CFD[25] can also be used to solve reactor problems. In recent years, Deep neural networks (DNN) have been more frequently used in the problem of reactor core[26, 27]. Among them, Liu Dong[28, 29] applied PINNs to solve multiple neutron diffusion benchmark equations and demonstrated highly accurate predictive results. By utilizing FCN to capture neutron distribution, they achieved a neutron flux distribution solution with an accuracy as high as e-07 and successfully applied it to the search for k_{eff} .

Moreover, FCNs are prone to gradient vanishing and can encounter non-convergence during training. When the gra-

* Supported by the Science and Technology on Reactor System Design Technology Laboratory (No.LRSdT12023108) and supported in part by the Chongqing Postdoctoral Science Foundation (No.cstc2021jcyj-bsh0252), the National Natural Science Foundation of China(No.12005030), Sichuan Province to unveil the list of marshal industry common technology research projects(23jBGOV0001) and Special Program for Stabilizing Support to Basic Research of National Basic Research Institutes(WDZC-2023-05-03-05)

† Corresponding author, Dong Liu, No. 328, Section 1, Changshun Avenue, Huayang, Shuangliu County, Chengdu, Sichuan, China, 13980956120, liudong73@yahoo.com

Table 1. Comparison Between PINN and Traditional Numerical Methods.

Feature	PINN	Traditional Numerical Methods
Calculation Method	Combines neural networks with physics equations	Uses analytical solutions or numerical methods
Accuracy Dependency	Data noise level, physics model accuracy	Grid resolution, numerical methods
Computational Efficiency	Low computational demand, training process needs hyperparameter optimization	High computational demand, requires significant computational resources
Reliability	Robust to data noise and uncertainty	Sensitive to initial conditions, boundary conditions, and numerical parameters
Model Complexity	Can handle complex nonlinear problems	Typically suitable for specific types and relatively simple problems
Training Speed	Relatively fast training speed. But adjusting model hyperparameters is time-consuming	High computational complexity, longer runtime
Grid Dependency	Grid-independent	Results are influenced by grid accuracy and partitioning
Parameter Tuning	Requires tuning of network architecture and hyperparameters	Requires tuning of grid partitioning and solver parameters
Parallel Computing Applicability	Efficient parallel computing Suitable for complex nonlinear problems and data scarcity	Has challenges in parallel computing Suitable for known fluid dynamics equations and stable boundary conditions

dient vanishes, NN parameters will not be updated and the network will find it hard to learn new knowledge[30]. This may lead to the network having difficulty converging to an optimal solution, missing a large amount of information, and affecting the expressive power of the model. In the aspect of solving the neutron diffusion equation, the error in the predicted result will further make the critical judgment inaccurate. Furthermore, observation found that regions with large gradients will exhibit insufficient training under uniform sampling, especially when the number of sampling points is limited, leading to significant errors in regions with large gradients, thereby limiting further improvement in network accuracy. During solving the neutron diffusion equation, the limited accuracy may lead to inefficient parameter searches that greatly increase search time.

Toward these challenges, recent studies propose adaptive sampling based on gradient information[31] and assigning adaptive weights to sample points in loss calculation[32, 33]. These enhancements improve the prediction performance of PINNs in regions with pronounced gradients and limited sampling points. Furthermore, the issue of gradient disappearance in FCNs remains unresolved. Researchers have explored replacing FCNs with other neural network techniques[34], such as CNNs[35] and RNNs[36], to achieve better performance and more precise results.

To this end, this paper proposes a novel framework called R²-PINN, which combines the S-CNN architecture with the RAR method to solve neutron diffusion equations. The proposed model, by adding the gradient backpropagation path, effectively alleviates the gradient vanishing problem. Moreover, with a resample mechanism, the network can balance the loss between regions and reach a higher accuracy. R²-PINN has been evaluated against the FCN for solving the neutron diffusion equation benchmark problems, which will be introduced in Section II, and shows that our method effectively suppresses loss function oscillation and achieves high-precision field prediction. In addition, our method signifi-

cantly reduces the time required for an eigenvalue search, allowing us to obtain an accuracy of e-05 within just 10 minutes and obtain an accuracy of e-04 in only the 250s.

The rest of this paper is organized as follows. Section II introduces benchmark problems using in Section IV, and Section III provides an introduction to the basic architectures, including the structure of S-CNN and RAR resample method and the overall R²-PINN architecture. Section IV provides multiple experiments to optimize hyperparameters and verify the superiority of the proposed model. Especially different search algorithms are compared for parameter search to try to reduce the search time. It also includes generalizability validation experiments using the same model for multiple benchmark problems. Then, Section V analyzes and discusses the results of the experiment. Finally, Section VI concludes our study and discusses future research directions.

II. PROBLEM SETUP

A. One-dimensional reactor diffusion equation for a single energy group

In this section, a single-group k-eigenvalue problem is introduced for criticality calculations. The largest value of k , known as the effective neutron multiplication factor or k_{eff} , needs to find out. The equation of the single-group neutron diffusion model is commonly denoted as Eq. 1.

$$\begin{aligned} \frac{1}{v} \frac{\partial \phi(r, E, t)}{\partial t} = & \nabla \cdot D \nabla \phi(r, E, t) - \Sigma_t(r, E) \phi(r, E, t) + \\ & x(E) \int_0^\infty \vartheta(E') \Sigma_f(r, E') \phi(r, E', t) dE' + \\ & S(r, E, t) + \int_0^\infty \Sigma_s(r, E' \rightarrow E) \phi(r, E', t) dE' \end{aligned} \quad (1)$$

Where $\phi(r, E, t)$ denotes the neutron flux of energy group E in the r -coordinate at the moment t , v represents the neutron velocity, D denotes the diffusion coefficient, ϑ represents neutrons per fission numbers, $x(E)$ represents prompt neutron spectra, Σ_t represents total macroscopic cross section, Σ_s represents macroscopic scattering cross section from group E' to group E , Σ_f represents fission macroscopic cross-section, and $S(r, E, t)$ represents the neutron source.

In the absence of $S(r, E, t)$, an initial neutron flux density is symmetric along the x -axis. Eq. 1 can be simplified into Eq. 2 [1].

$$\frac{1}{Dv} \frac{\partial \phi(r, t)}{\partial t} = \nabla^2 \phi(r, t) + \frac{k_\infty - 1}{L^2} \phi(r, t) \quad (2)$$

Here, k_∞ represents the infinite multiplication factor, and L^2 denotes the diffusion length. Consider a uniform bare reactor[40], which is shaped as an infinite plate bare reactor with dimensions of infinite length and width and a thickness (including extrapolation distance) of a , as illustrated in Fig. 1. The analytical solution for the neutron flux can be obtained using the method of separation of variables, as given by Eq. 3.

$$\phi(x, t) = \sum_{n=1}^{\infty} \left[\frac{2}{a} \int_{-\frac{a}{2}}^{\frac{a}{2}} \phi_0(x') \cos \frac{(2n-1)\pi}{a} x' dx' \right] \cos \frac{(2n-1)\pi}{a} x e^{(k_n-1)t/l_n} \quad (3)$$

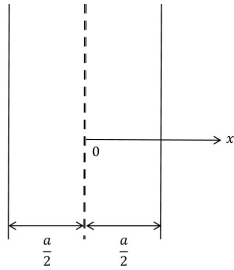


Fig. 1. Infinite Plate Reactor.

The critical condition for the bare reactor in the single-group approximation is given by Eq. 4.

$$k_{eff} = \frac{k_\infty}{1 + L^2 B^2} = 1 \quad (4)$$

Here, k_{eff} represents the effective neutron multiplication factor. When the system is in the criticality state, the neutron flux density distribution will satisfy the wave equation according to the fundamental eigenfunction corresponding to the minimum eigenvalue B_g^2 , as given by Eq. 5.

$$\nabla^2 \phi(r) + B_g^2 \phi(r) = 0 \quad (5)$$

If the composition of the system's materials (i.e., k_∞ and L^2) is given, a unique critical size, denoted as a_0 , makes

$k_{eff} = 1$. The critical size a_0 corresponds to the reactor being in a critical state. For reactor sizes larger than a_0 , $k_{eff} > 1$ indicates the reactor is in a supercritical state. Conversely, for reactor sizes smaller than a_0 , $k_{eff} < 1$, indicating the reactor is in a subcritical state[41]. On the other hand, if the reactor size is given, it is always possible to find a fuel enrichment (material composition) that satisfies Eq. 4 and ensures the reactor reaches criticality. When the system is in a critical state, the neutron flux density distribution within the reactor can be described as follows:

$$\phi(x) = A \cos \frac{\pi}{a} x \quad (6)$$

B. Two-dimensional reactor diffusion equation for a single energy group

Based on II A, consider the two-dimensional neutron diffusion equation, formulated as follows:

$$\frac{1}{Dv} \frac{\partial \phi(x, y, t)}{\partial t} = \nabla^2 \phi(x, y, t) + \frac{k_\infty - 1}{L^2} \phi(x, y, t) \quad (7)$$

By discretizing Eq. 7 and approximating the Laplace operator and the partial derivatives, the equation can be converted to the following form:

$$\frac{1}{Dv} \frac{\phi_{i,j}^{n+1} - \phi_{i,j}^n}{\Delta t} = \frac{\phi_{i+1,j}^n - 2\phi_{i,j}^n + \phi_{i-1,j}^n}{\Delta x^2} + \frac{\phi_{i,j+1}^n - 2\phi_{i,j}^n + \phi_{i,j-1}^n}{\Delta y^2} + \frac{k_\infty - 1}{L^2} \phi_{i,j}^n \quad (8)$$

Where $\phi_{i,j}^n$ denotes the value of neutron flux at the spatial grid point (i, j) at time n . Δt is the time step, Δx and Δy are the spatial steps in the x and y directions, respectively. D is the diffusion coefficient and v is the neutron velocity k_∞ denote the infinite multiplication factor, and L is the diffusion length.

According to Eq. 8, the spatial domain meshes use the finite difference method to solve for the entire domain flux magnitude, and the numerically solved data are used as a test set to verify the model accuracy.

C. Two-dimensional rectangular geometry multigroup multi-material diffusion problem

In a nuclear reactor, neutron transport can be described by the multigroup diffusion theory. In this case, the fast and hot group neutron fluxes satisfy the following diffusion equations:

$$-\nabla \cdot (D_1 \nabla \phi_1) + \Sigma_{r1} \phi_1 = \nu \Sigma_{f1} \phi_1 \quad (9)$$

$$-\nabla \cdot (D_2 \nabla \phi_2) + \Sigma_{r2} \phi_2 = \Sigma_{s1 \rightarrow 2} \phi_1 \quad (10)$$

Where D_1 and D_2 are the diffusion coefficients of the fast and hot group neutrons, respectively. ϕ_1 and ϕ_2 are the fast group and thermal group neutron flux densities, respectively. Σ_{r1} and Σ_{r2} are the macroscopic cross sections of fast group and hot group neutrons, respectively. ν is the neutron yield. Σ_{f1} is the fast group nuclear fission cross-section, and $\Sigma_{s1 \rightarrow 2}$ is the fast group to thermal group fission source term.

For pressurized water reactors, the two-group diffusion are satisfied Eq. 11 and Eq. 12, the example is divided into two different material regions, which is shown in Fig. 2, and the material parameters of each region are shown in Table. 2.

$$-D_1 \nabla^2 \phi_1(r) + \Sigma_{r1} \phi_1(r) = \frac{1}{k_{\text{eff}}} [v \Sigma_{f,1} \phi_1(r) + v \Sigma_{f,2} \phi_2(r)] \quad (11)$$

$$-D_2 \nabla^2 \phi_2(r) + \Sigma_{a2} \phi_2(r) = \Sigma_{1 \rightarrow 2} \phi_1(r) \quad (12)$$

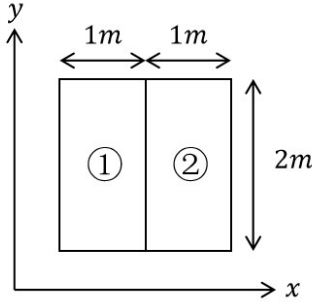


Fig. 2. Material Distribution[29].

Table 2. Calculate Area Material Properties.

Energy Group	Material 1		Material 2	
	1	2	1	2
$D_g(\text{cm})$	1.268	0.1902	1.255	0.211
$\Sigma_a(\text{cm}^{-1})$	0.007181	0.07047	0.008252	0.1003
$\nu \Sigma_f(\text{cm}^{-1})$	0.004609	0.08675	0.004602	0.1091
$\Sigma_{1 \rightarrow 2}(\text{cm}^{-1})$	0.02767	-	0.02533	-

Based on the multigroup diffusion theory, the distribution of neutron flux in the core is obtained by iteratively solving the discretized diffusion equation. The obtained dataset will be used as a test set in the experimental part to evaluate the model prediction accuracy.

D. 2D-IAEA benchmark problem

The 2D-IAEA PWR benchmark problem is a two-dimensional statics problem with two neutron groups but with no delayed neutron precursors[42], which modeled by two-dimension two-group diffusion equations below:

$$\begin{cases} -D_1 \nabla^2 \phi_1 + (\Sigma_{a,1} + \Sigma_{1 \rightarrow 2}) \phi_1 = \lambda \chi_1 (\nu \Sigma_{f,1} \phi_1 + \nu \Sigma_{f,2} \phi_2) \\ -D_2 \nabla^2 \phi_2 + \Sigma_{a,2} \phi_2 - \Sigma_{1 \rightarrow 2} \phi_1 = \lambda \chi_2 (\nu \Sigma_{f,1} \phi_1 + \nu \Sigma_{f,2} \phi_2) \end{cases} \quad (13)$$

The reactor has a two-zone core containing 177 fuel assemblies which are 20 cm in width. The core is reflected radially by 20 cm of water. Due to the symmetry along the x and y axis, This one quarter reactor domain is denoted by Ω and it is composed of four sub-regions of different physical properties which are $\Omega_{1,2,3,4}$. The reactor is depicted in Fig. 3. Neumann boundary conditions are enforced on the left and the bottom boundaries. The group constants for this problem are given in Table. 3.

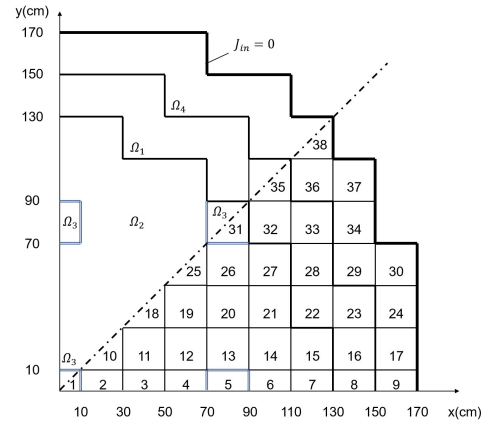


Fig. 3. Geometric layout of the 2D-IAEA benchmark problem[42].

Table 3. Group constants of the 2D-IAEA benchmark.

Region	Group	$D_g(\text{cm})$	$\Sigma_{a,g}(\text{cm}^{-1})$	$\nu \Sigma_{f,g}(\text{cm}^{-1})$	$\Sigma_{1 \rightarrow 2}(\text{cm}^{-1})$
Ω_1	1	1.5	0.010	0.000	0.02
	2	0.4	0.080	0.135	
Ω_2	1	1.5	0.010	0.000	0.02
	2	0.4	0.085	0.135	
Ω_3	1	1.5	0.010	0.000	0.02
	2	0.4	0.130	0.135	
Ω_4	1	2.0	0.000	0.000	0.04
	2	0.3	0.010	0.000	

III. METHODS

A. PINN Loss Formulation

In PINN, considering the general form of a parameterized and nonlinear PDE:

$$F(u, x, y, t, :) = 0, (x, y) \in \Omega, t \in [0, T] \quad (14)$$

Where u represents the latent solution, and Ω represents the solution domain. This formula can express PDEs in almost all fields of mathematical physics.

N_f data points are sampled to measure physical consistency. This type of loss will be collectively referred to as the PDE loss in the following form:

$$Loss_{PDE} = \frac{1}{N_f} \sum_{i=1}^{N_f} F(u, x, y, t, :); x \in \Omega \quad (15)$$

Then, through the introduction of initial loss and boundary loss due to the known initial and boundary conditions. N_i and N_b data points are collected for calculating $Loss_{Initial}$ and $Loss_{Boundary}$ respectively. Meanwhile, a few data need to be used for training.

$$Loss_{Initial} = \frac{1}{N_i} \sum_{i=1}^{N_i} (\phi_{truth} - \phi_{predict}); t = 0, x \in \Omega \quad (16)$$

$$Loss_{Boundary} = \frac{1}{N_b} \sum_{i=1}^{N_b} (\phi_{truth} - \phi_{predict}); x \in \partial\Omega \quad (17)$$

$$Loss_{Data} = \frac{1}{N_d} \sum_{i=1}^{N_d} (\phi_{truth} - \phi_{predict}) \quad (18)$$

Incorporating a small amount of labeled data provides information about the correct order of magnitude, enabling the PINN to better calibrate its predictions and avoid unrealistic or divergent solutions. The inclusion of such labeled data greatly contributes to the stability and accuracy of the training process for PINNs. By combining the losses above, networks can be penalized and the training process effectively constrained, thereby ensuring that the obtained solutions adhere more closely to the fundamental laws of physics. Therefore, the final network loss formulation is as follows:

$$Loss_{Total} = Loss_{PDE} + (Loss_{Initial} + Loss_{Boundary} + Loss_{Data}) \cdot w \quad (19)$$

The sampling ratio for the PDE loss, boundary loss, initial loss and data loss is approximately 30:10:10:1. Multiple losses can be balanced by adjusting weights w , preventing the network from prioritizing a single loss, especially when significant differences in magnitude between losses exist.

B. S-CNN Architecture

In solving the neutron diffusion equation, the performance of NN can be significantly affected by the vanishing gradient problem as the network depth increases. This problem can easily lead to training failure and make the result unreliable.

Moreover, it greatly limits the growth of the number of layers, reduces the expressive power of the network, and limits the prediction accuracy of the network. Inspired by the effective alleviation of the gradient vanishing problem in ResNet architecture[43] in the image domain, which introduces the concept of residual learning, enables networks to learn residual mappings (the difference between input and desired output), making it easier to train very deep neural networks. The skip connection mechanism is introduced into the PINN architecture.

The input sampling features are coordinates, namely x , y , and t , which are independent. So the experiment applies a separate filter to each feature. A one-dimensional convolution is used as the basis for each network layer. Each hidden layer follows the following formula:

$$z_l = f_l(W_l z_{l-1} + b_l) \quad (20)$$

Where z_l denotes the hidden layer l between the input and output layers, W_l and b_l are the weight and bias, respectively; $f_l(\cdot)$ denotes the activation function (e.g., tanh function.).

On this basis, some skip connections are added between different layers. The corresponding hidden layer can be represented as follows:

$$z_l = f_l((W_l z_{l-1} + b_l) + z_{l-n-1}), l > n + 1 \quad (21)$$

Where n represents the skip distance, i.e., how many hidden layers are crossed. To determine where the skip connection should be added, the contribution of each layer to the training of the whole network is measured by calculating the gradient norm for each layer. Where the gradient norm is computed as follows[39]:

$$\|g\| = \text{sqrt}(\text{sum}(g_i^2)) \quad (22)$$

For example, in the 10-layer network, the gradient contribution is calculated for each layer of the network, as shown in Fig. 4.

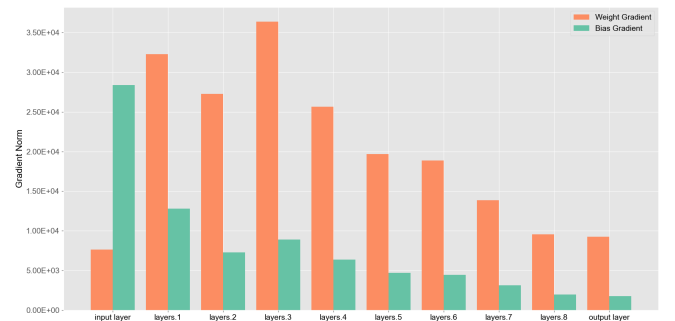


Fig. 4. Gradient Norm of Each Layer.

When the gradient is more significant, it indicates that the layer's parameters can be easily updated. A too-large gradient will result in an unstable model, and a too-small gradient

indicates that the layer may need to go through more iterations to reach the optimal state and may face the gradient vanishing problem. Thus, the network increases the shallow gradient paths by establishing shallow-to-deep skip connections, providing more gradient paths in shallow layers and avoiding vanishing gradients in deep layers. The detailed 10-layer S-CNN architecture used in Section IV is shown in Table 4, where B, C, and L represent the batch size, channel, and length.

Table 4. S-CNN Structure.

Layer Name	Input Size(B,C,L)	Output Size(B,C,L)	Param
input layer	(None,2,1)	(None,26,1)	78
conv1 layer	(None,26,1)	(None,26,1)	702
conv2 layer	(None,26,1)	(None,26,1)	702
conv3 layer	(None,26,1)	(None,26,1)	702
conv4 layer	(None,26,1)	(None,26,1)	702
conv5 layer	(None,26,1)	(None,26,1)	702
conv6 layer	(None,26,1)	(None,26,1)	702
conv7 layer	(None,26,1)	(None,26,1)	702
conv8 layer	(None,26,1)	(None,26,1)	702
output layer	(None,26,1)	(None,1,1)	27

In the experimental section, the skip distance n is set to 2 for larger spans of gradient propagation, which is the best parameter for shallow networks. when $n < 2$, the jump distance is insufficient, which may limit the network's ability to learn complex physical fields and does little to avoid the gradient vanishing problem, and when $n > 2$, the number of jumping layers is too large, which may pose a challenge to gradient propagation and thus increase the difficulty of optimizing the network. Experiments are conducted on S-CNN models with varying depths, and high-precision results are consistently obtained, thus validating the effectiveness of the residual module in addressing the gradient problem.

C. RAR Mechanism

Due to specific regions with large gradients in the overall solution domain, if sampled uniformly, the network suffers from inadequate fitting of local regions. This issue can be addressed by increasing the weights of specific sampling points, as shown in Eq. 23, or by resampling using Eq. 24.

$$X_{new} = X_{raw} + w \cdot X_f \quad (23)$$

$$X_{new} = X_{raw} + X_{resample} \quad (24)$$

Here, X_{raw} represents the original dataset, X_{new} represents the new dataset, X_f represents the set of sampling points with more significant PDE residuals, $X_{resample}$ represents the set of resampling points, and w represents the penalty weight.

Meanwhile, referring to the grid division of traditional numerical computation methods, finer-grained samples should be collected in regions with large gradients to improve the network's prediction accuracy in this region.

Based on this, consider using Eq. 24 to update our dataset, i.e., introducing RAR[37] to improve the distribution of residual points during the training process of PINNs to address the bottleneck phenomenon that arises from the difficulty of reducing PDE residuals in certain regions, ultimately enhancing the predictive accuracy of the model.

By selectively sampling more points in regions where the PDE residuals are more significant, this approach allows the network to focus on challenging areas and adjust the sampling density accordingly, leading to improved learning and prediction capabilities. The method is particularly effective in capturing the complex behavior of the PDE solution and identifying sharp gradient regions.

The specific pseudo code for the RAR method is as follows:

Algorithm 1: RAR Algorithm.

Input : Set S with randomly sampled initial points

Output: Updated set S

Divide solution domain into α^2 subintervals;

Train PINN for n iterations;

repeat

 Compute $Loss_{PDE}$ for the points in set S ;

 Calculate the average residual of each subinterval;

 Randomly sample S' from the subinterval with the highest average residual;

 Update set S : $S = S \cup S'$;

 Train PINN for n iterations;

until the maximum number of iterations is reached or the total number of points reaches the limit;

This algorithm divides the solution domain into α^2 subintervals, with α subdivisions in both the x and t directions. The Latin Hypercube Sampling (LHS) method[38] is used for random sampling, which ensures sample points cover the entire space without clustering or bias.

As shown in Fig. 5, by adaptively adding points in regions with more significant residuals, more intensive sampling has been conducted in one of the subdomains of the entire domain. This enables the network to capture the PDE solution's behavior better. This adaptive sampling approach improves the distribution of residual points and mitigates the bottleneck phenomenon, ultimately enhancing the accuracy and performance of the model and speeding up the model convergence.

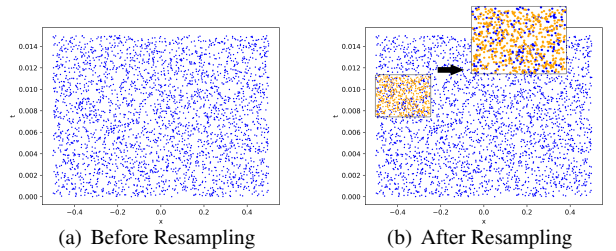


Fig. 5. PDE Points Distribution.

D. Proposed Framework:R²-PINN

Our paper proposes the R²-PINN architecture, which combines the PINN structure, S-CNN, and RAR mechanism to solve PDEs with improved accuracy and computational efficiency.

The structure of R²-PINN is shown in Fig. 6. In R²-PINN, the S-CNN is used as the backbone of the network, which can better capture the features of the PDE solution and improve the training efficiency. The RAR mechanism is employed to balance $Loss_{PDE}$ across different regions of the domain, ensuring that the network focuses on regions with high errors and adaptively refines the mesh.

By combining the PINN structure, S-CNN, and RAR mechanism, R²-PINN can effectively solve PDEs with improved accuracy and computational efficiency. It leverages the power of deep learning and adaptive refinement to capture complex features of the PDE solution, enabling a more precise representation of physical phenomena. Section IV will verify the superiority of the proposed R²-PINN network and each mechanism through a series of experiments.

IV. EXPERIMENTS

In Section IV A, the generation of datasets is introduced specifically for testing accuracy. Section IV B, through comparing S-CNN networks with different depths to validate the superiority of the improved PINN network architecture. Section IV C investigated how resampling affects the model's accuracy. In Section IV D, R²-PINN is implemented to search for k_{eff} and enhance search efficiency, discussed in Section IV E. Lastly, in Section IV F, the generalization capabilities of the improved PINN architecture model are tested. Furthermore, Sections IV G to IV I explore the generalizability of models in two-dimensional neutron diffusion, including multi-group and multi-material scenarios.

A. Dataset Preparation

1. One-dimensional reactor diffusion equation for a single energy group

According to Eq. 3 and the assumption of symmetric initial conditions, two initial distributions are used for the dataset:

$$\begin{aligned}\phi_1(x, 0) &= \cos(\pi \cdot x/a) - 0.4\cos(2\pi \cdot x/a) - 0.4; \\ \phi_2(x, 0) &= 0.5\cos(2\pi \cdot x/a) + 0.5; \\ x &\in [-0.5, 0.5]\end{aligned}\quad (25)$$

The specific numerical values used for the Eq. 3 are as follows: $\nu = 2.2 \times 10^3 \text{m/s}$, $D = 0.211 \times 10^{-2} \text{m}$, $L^2 = 2.1037 \times 10^{-4} \text{m}^2$, $a = 1 \text{m}$. The boundary follows the Delicacy boundary and predicts the flux distribution for 0.015s. By changing the k_∞ parameter value, data can be obtained on how the flux varies with time for different parameter settings.

Our test dataset consists of 10000 data points with 100 grid points in both the x and t directions. The experimental part will test the model prediction accuracy on this dataset.

2. Two-dimensional reactor diffusion equation for a single energy group

To ensure that the boundary flux is 0 and the full domain flux is continuous, we set the initial flux distribution at the time $t = 0$ to the following equation:

$$\begin{aligned}\phi &= (\exp(-(x^2 + y^2)/20) - \exp(-100)) \\ x &\in [-10, 10], y \in [-10, 10].\end{aligned}\quad (26)$$

An iterative solution was performed using a time step Δt of 0.001 with a grid number of 100 in the x, y, t direction to solve for the flux distribution for 1 second, which was used as a dataset for testing the model.

3. Two-dimensional rectangular geometry multigroup multi-material diffusion problem

A source iteration method is used to solve for the dual-group neutron flux and is used to test the model's accuracy. The range of values of x, y is shown in Fig. 2. And total dataset consists of 10000 data points with 100 grid points in both the x and y directions and the boundary follows the Delicacy boundary.

4. 2D-IAEA problem

The reference solution for the two-dimensional, two-group diffusion equations is obtained using the high-quality, general-purpose finite element solver FreeFem++[44]. The eigenvalue problem is solved using tools from arpack++, the object-oriented version of the ARPACK eigenvalue package[45]. The total number of samples in the dataset is 12286[46], using 76 of the data points as data feed into the network, and finally all the samples in the dataset are used to validate the model accuracy.

B. S-CNN Depth and Kernel Size Ablation Experiment

All parameters except the base network are kept consistent to compare the FCN architecture with the S-CNN architecture. The total number of sampled data points is 5000, with 3000 data points used to calculate the $Loss_{PDE}$, and 1000 data points sampled for the $Loss_{Initial}$ and $Loss_{Boundary}$, respectively. The network training does not involve feeding data to calculate $Loss_{data}$. Tanh activation function and LBFGS optimizer are used, and the Gaussian distribution random sampling method is used to initialize the network weights and biases. The number of hidden neurons per layer in the network is set to 26.

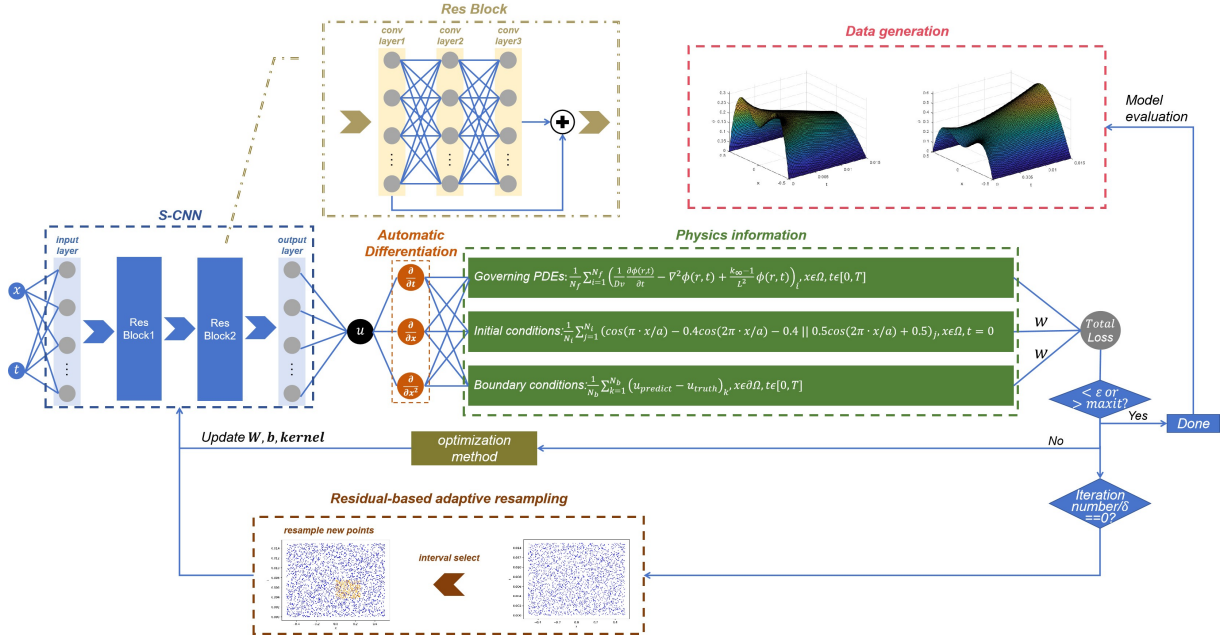


Fig. 6. Overall Architecture.

To investigate the impact of layer numbers and kernel size on model performance, ablation experiments were conducted on S-CNN networks with different depths and different kernel sizes. For kernel size 1, the padding was set to 0; for kernel size 3, the padding was set to 1. The detailed experimental results are shown in Table 5 and Fig. 7.

In Table 5 and Fig. 7, Ω MSE refers to the MSE score over the entire domain, and Ω_1 MSE refers to the MSE score at $t = 0.015s$, which is calculated separately to assess the model's ability to extrapolate in time. Baseline refers to the result of FCN.

Based on Table 5 and Fig. 7, it can be observed that when layer numbers are lower than 10, the accuracy shows a positive correlation with layer numbers. But as the layer number further increases, the accuracy cannot reach higher. Hence, it is better to choose fewer layer numbers to make the NN train faster and achieve high accuracy. This is because the expressive ability of the neural network increases as the number of layers increases, but beyond a certain threshold, the increase in the number of layers does not significantly improve the expressive ability of the network; the increase in the number of layers only increases the training time consumed, and the model suffers from overfitting problems. Moreover, Because the input features are coordinates and have no relation to each other, the kernel size set to 1 can consider each channel as an independent feature to tackle, and this operation is more in line with reality. So, a kernel size set to 1 can achieve higher accuracy than a kernel size set to 3. Based on the above analysis, the 10-layer S-CNN with a kernel size of 1 exhibits the best predictive accuracy with a minimum number of parameters. Consequently, this configuration will be utilized for subsequent experiments.

C. Ablation Experiment on Resampling Parameters in S-CNN

According to the RAR algorithm, the resampling granularity is set to α to define the granularity of the subdomains in the solution domain. The solution domain is divided into α subintervals along the x and t dimensions, resulting in α^2 subintervals. Following the RAR algorithm, every 1000 epochs, the network calculates and compares the MSEs of each subdomain and performs resampling in the subinterval with the largest MSE. The number of resampling points is denoted as m .

The initial PDE sampling point is set to 3000 to avoid excessive sampling and training time. Moreover, 2000 data points are sampled, with 1000 points to calculate the initial loss and 1000 points to calculate the boundary loss. The maximum number of PDE samples is set to 5000, and resampling stops when the total number of PDE samples reaches 5000 after multiple iterations. The LHS method is used for each sampling.

Ablation experiments are conducted from two dimensions: the resampling granularity and the number of resampling points while maintaining the same S-CNN architecture (10 layers) and other hyperparameters. The S-CNN network is compared with an FCN network (baseline) using the same initial condition, i.e. $\phi_0 = \phi_1$. The detailed experimental results are shown in Table 6 and Table 7.

From Table 6 and Table 7, it is evident that under different sampling hyperparameters, our network consistently achieves a better Ω_1 MSE result that is two orders of magnitude higher than the FCN baseline. When using the optimal hyperparameters, R²-PINN can achieve an e-08 or even e-09 accuracy. This indicates that our method has a significant advantage in determining whether the flux values reach a steady state at a

Table 5. Ablation Study on S-CNN Depth and Kernel Size.

S-CNN Layer	k=1.0041 ($\phi_0 = \phi_1$)				k=1.0001 ($\phi_0 = \phi_2$)			
	Kernel Size=1		Kernel Size=3		Kernel Size=1		Kernel Size=3	
	Ω MSE	Ω_1 MSE	Ω MSE	Ω_1 MSE	Ω MSE	Ω_1 MSE	Ω MSE	Ω_1 MSE
Baseline	8.9×10^{-7}	3.8×10^{-6}	8.9×10^{-7}	3.8×10^{-6}	4.4×10^{-6}	1.8×10^{-5}	4.4×10^{-6}	1.8×10^{-5}
6	1.2×10^{-7}	3.1×10^{-8}	1.4×10^{-7}	6.2×10^{-8}	2.4×10^{-7}	1.6×10^{-7}	1.4×10^{-7}	2.1×10^{-7}
7	1.5×10^{-7}	5.4×10^{-8}	1.4×10^{-7}	6.5×10^{-8}	1.8×10^{-7}	1.3×10^{-7}	1.7×10^{-7}	1.6×10^{-7}
8	9.6×10^{-8}	2.6×10^{-8}	1.4×10^{-7}	6.5×10^{-8}	1.8×10^{-7}	1.3×10^{-7}	1.7×10^{-7}	1.6×10^{-7}
9	9.9×10^{-8}	3.9×10^{-8}	3.9×10^{-7}	6.6×10^{-8}	1.1×10^{-7}	3.1×10^{-8}	3.6×10^{-7}	2.0×10^{-8}
10	8.3×10^{-8}	4.0×10^{-8}	2.2×10^{-7}	3.9×10^{-8}	5.8×10^{-8}	1.9×10^{-8}	8.8×10^{-7}	3.4×10^{-7}
11	1.6×10^{-7}	1.4×10^{-7}	2.2×10^{-7}	7.4×10^{-8}	5.8×10^{-8}	2.8×10^{-8}	6.8×10^{-6}	6.3×10^{-6}
12	2.1×10^{-7}	1.2×10^{-7}	3.5×10^{-7}	6.1×10^{-7}	2.3×10^{-7}	3.2×10^{-7}	2.6×10^{-7}	2.7×10^{-7}
13	1.3×10^{-7}	1.1×10^{-7}	5.1×10^{-7}	6.0×10^{-7}	8.1×10^{-8}	9.3×10^{-8}	1.8×10^{-7}	3.1×10^{-8}
14	1.5×10^{-6}	1.4×10^{-7}	4.3×10^{-7}	1.2×10^{-6}	1.8×10^{-7}	2.7×10^{-7}	1.3×10^{-7}	1.4×10^{-7}
15	1.6×10^{-7}	1.1×10^{-7}	4.4×10^{-7}	1.3×10^{-6}	1.3×10^{-7}	2.9×10^{-8}	1.4×10^{-7}	5.2×10^{-8}
16	1.5×10^{-7}	9.7×10^{-8}	1.7×10^{-7}	1.7×10^{-7}	1.9×10^{-7}	2.6×10^{-8}	3.0×10^{-7}	5.8×10^{-8}

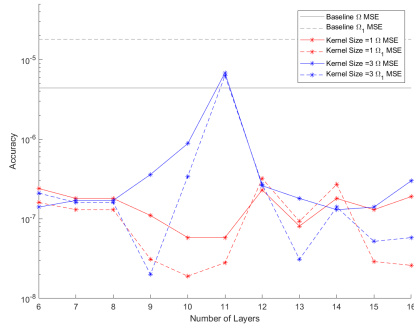
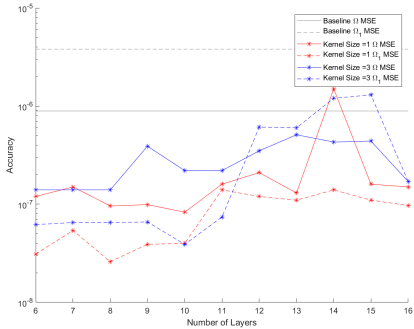
(a) $\phi_0 = \phi_1$ (b) $\phi_0 = \phi_2$

Fig. 7. Comparative Accuracy with Different Model Parameters.

specific moment. This advantage will also be demonstrated during the k_{eff} search in Section IV D.

Furthermore, the results are obtained by adopting another initial condition where $\phi_0 = \phi_2$. Then, a boxplot analysis on the resampling hyperparameters for all the results, which are shown in Fig. 8 and Fig. 9. It can be observed that when the number of resamples is 500 and the resample granularity is set to 2, the model can reach the best accuracy.

Table 6. Ablation Study on Resampling Numbers.

Resample Numbers m	Ω MSE	Ω_1 MSE
Baseline	8.9×10^{-7}	3.8×10^{-6}
0	9.1×10^{-8}	2.1×10^{-8}
100	1.3×10^{-7}	8.4×10^{-8}
200	9.5×10^{-8}	9.8×10^{-9}
300	1.3×10^{-7}	5.4×10^{-8}
400	9.8×10^{-8}	4.1×10^{-8}
500	8.0×10^{-8}	4.9×10^{-9}
600	1.3×10^{-7}	3.1×10^{-8}
700	1.0×10^{-7}	2.0×10^{-8}
800	3.9×10^{-8}	1.8×10^{-8}

Table 7. Ablation Study on Resampling Granularity.

Resample Granularity α	Ω MSE	Ω_1 MSE
Baseline	8.9×10^{-7}	3.8×10^{-6}
2	8.0×10^{-8}	4.9×10^{-9}
3	1.5×10^{-7}	8.5×10^{-8}
4	1.2×10^{-8}	9.1×10^{-8}
5	6.4×10^{-7}	3.5×10^{-8}
6	1.0×10^{-7}	8.8×10^{-8}

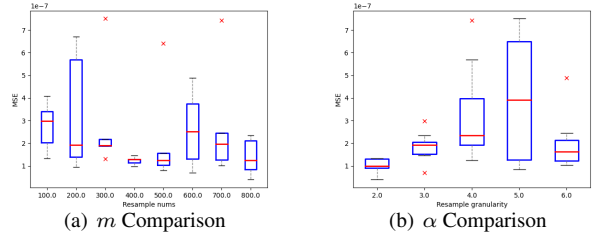


Fig. 9. MSE Comparison Between Parameters.

Given the introduction of the RAR mechanism, it is necessary to consider whether there is a large time overhead. Hence, time comparisons are performed for different numbers of samples, the results of which are shown in Fig. 8. It can be observed that when the number of resamplings is

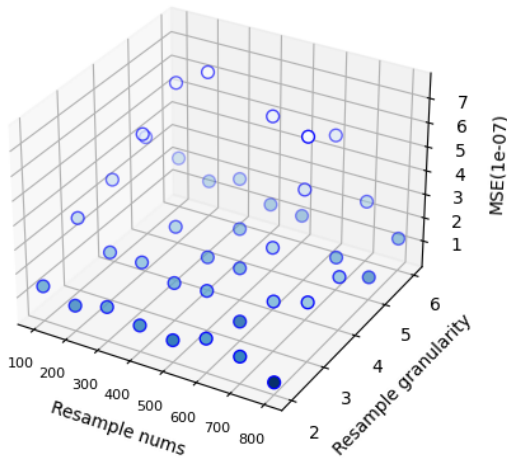


Fig. 8. Resample Parameter 3D Visualization.

set to 500, the training time required by the model is significantly reduced as compared to setting the number of resamplings to zero. By calculating the time consumed per cycle, we find that the trend does not increase significantly. Thus, setting the appropriate number of resamplings effectively reduces the overall network training time. This shows that the RAR method has an increase in the number of sampling points, leading to a different density of samples in each region as well as a relatively large number of sampling points in complex regions, which greatly contributes to the convergence speed of the network.

Table 8. Training Performance with Different Resample Numbers.

m	Training Epochs	Training Time (s)	Avg. Time per Epoch(s)
0	3262	275.28	0.084
100	3875	300.36	0.078
200	1005	84.25	0.084
300	2004	174.32	0.087
400	2544	164.16	0.065
500	1004	84.48	0.084
600	3004	240.74	0.080
700	3004	287.95	0.096
800	2005	140.02	0.070

The model uses the optimal resampling parameter configuration to predict the flux distribution under different k_∞ values where $\phi_0 = \phi_1$, the error plot is shown in Fig. 10. Except for the relatively large errors at $t = 0$, the errors in other regions are relatively flat. Notably, as time increases, the errors show a slight increase. In addition, Fig. 11 shows the distribution of predicted values by the model. It can be observed that when t approaches 0, there is a specific deviation between the data in the boundary region and 0. This guides us to appropriately increase the weights of boundary loss and initial condition loss.

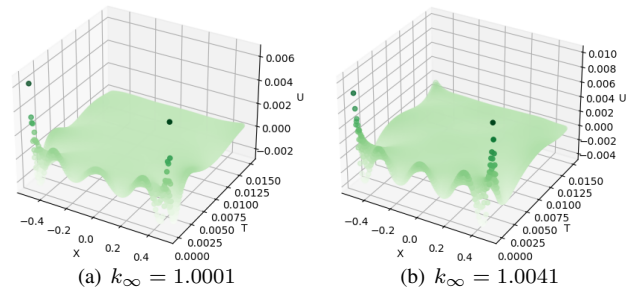


Fig. 10. Error Field.

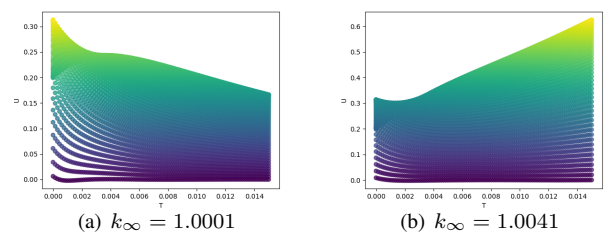


Fig. 11. Predict Result.

To evaluate the model's performance and measure the difference between losses, Fig. 12 show the training and test losses separately. In Fig. 12, $Loss_{PDE}$ is bigger than $Loss_{Boundary}$ and $Loss_{Initial}$, this may lead to $Loss_{PDE}$ dominate the optimization process and other losses cannot be optimized well. To address this issue, w in Eq. 19 is set to 100 to impose greater penalties on the boundary and the initial region error. R^2 -PINN can converge in just 2000 epochs.

Based on experiment results in Section IV B and Section IV C, an optimized S-CNN architecture with optimized RAR mechanism is used to compose the R^2 -PINN to further used to search k_{eff} , which will conduct in Section IV D and Section IV E.

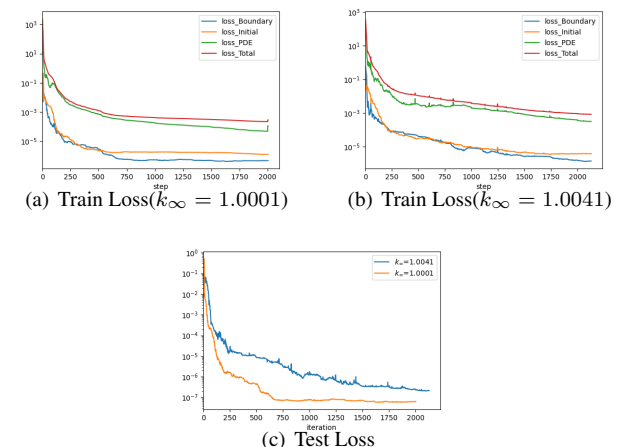


Fig. 12. Loss Over Iterations.

D. k_{eff} Search with R²-PINN

For a given geometric shape and volume of the reactor core, k_∞ and L^2 can be adjusted by modifying the reactor core size or changing the composition of materials within the reactor so that k_{eff} equals 1. When the system reaches a steady state after a sufficient period, the neutron flux density follows the distribution described by Eq. 6, and the reactor will be in a critical state.

In this experiment, maintain the L^2 parameter size unchanged and train different networks by adjusting k_∞ to predict the evolution of neutron flux at this parameter. By continuously adjusting the value of the k_∞ parameter, try to adjust k_{eff} to 1, reaching a critical state. Initially, the parameter search range is set to [1.0001, 1.0041]. It has been verified that when k_∞ is 1.0001, $k_{eff} < 1$, indicating a subcritical state, where $\phi(x, t)$ exponentially decays with time t . When k_∞ is 1.0041, $k_{eff} > 1$ indicates a supercritical state, where $\phi(x, t)$ continuously increases. The specific distribution figure is shown in Fig. 13.

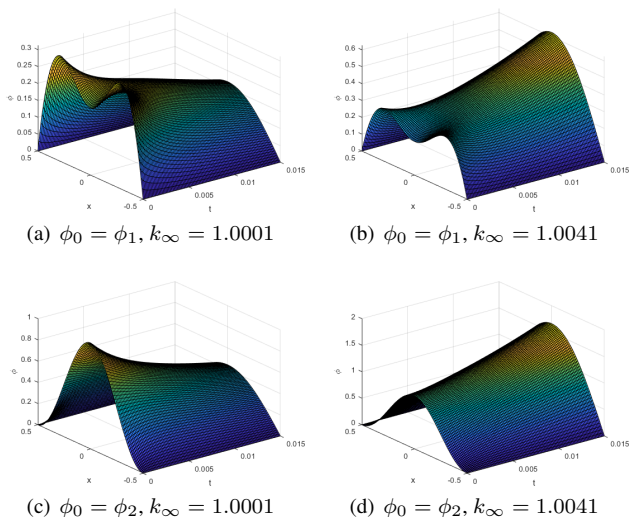


Fig. 13. ϕ Distribution.

In the absence of delayed neutrons, when the system approaches criticality, regardless of different boundary conditions, the system will converge to a critical state within a very short time (5-8ms), where ϕ remains unchanged. At this point, the ϕ distribution is the steady-state analytical solution. The interval is partitioned into n equal parts and obtains multiple k_∞ values. The network is trained for each value, calculates ϕ_t after a specific time t_τ , and performs a search until ϕ_t tends to zero within an acceptable accuracy range. The specific process is illustrated in Fig. 14.

In each network, Eq. 2 is used as the equation for $Loss_{PDE}$. Eq. 25 is used as the equation for $Loss_{Initial}$ and calculates the mean squared error (MSE) between the predicted values and 0, which serves as the $Loss_{Boundary}$.

Using the automatic differentiation mechanism of NN, the partial derivative of ϕ concerning t is calculated after obtain-

ing the predicted values. Given the network's ability to predict flux variations within the time interval of 0.015s, the experiment uses the last five time points to calculate $\partial\phi(r, t)/\partial t$ and determine whether the system is in a critical state [28].

Using Fig. 14, the searches for the k_{eff} when the initial distribution follows ϕ_1 and ϕ_2 are conducted and record each search result. The ϕ_t as a function of k is shown in Fig. 15. When $n = 2$ and the grid method degenerates into a binary search, it only takes about 20 iterations to obtain the search results with an accuracy level of e-05. The total runtime for the program is approximately 30 minutes.

From Fig. 15, ϕ_t changes exponentially with k_∞ . This further suggests that gradient-based methods such as gradient descent or Newton's method can be explored to search for parameter values more quickly and efficiently. Alternatively, using curve fitting techniques to fit the scattered data and the intersection of the resulting curve with the x-axis gives the parameter value k_∞ at the critical state. This may finish within a low number of search iterations. The k_∞ value corresponding to the critical state can be identified by progressively refining the intervals. Search results are shown in Table 9. Among them, $\Delta\phi$ in the last five time points were recorded to measure whether ϕ reaches a steady state. Compared with the result of FCN[28], R²-PINN has a smaller $\Delta\phi$, and this means R²-PINN search has higher accuracy than FCN. Further, the search results are validated by generating the ϕ distribution for the obtained k_∞ value, which are shown in Fig. 16.

Table 9. Search Result.

	$\phi_0 = \phi_1$		$\phi_0 = \phi_2$	
	k_∞	$\Delta\phi$	k_∞	$\Delta\phi$
FCN	1.00202	-0.017973	0.99803	-0.788704
R ² -PINN	1.0020822	-0.001522	1.0020824	-0.001519

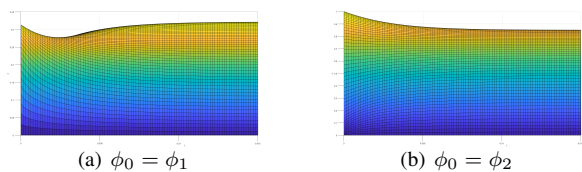


Fig. 16. Steady-State Verification.

From Fig. 16, it can be observed that the flux tends to stabilize as t increases, indicating that the system reaches a critical state. This indicates that our network can effectively search for the optimal parameters corresponding to the critical state.

E. k_{eff} Search Efficiency Improvement

When starting to search the k_{eff} , the initial search interval is large. The k -value to be searched is far away from the critical state k -value. Thus, the accuracy of prediction is not highly required; only use the prediction to compute ϕ_t to serve as a priori information for the next interval refinement.

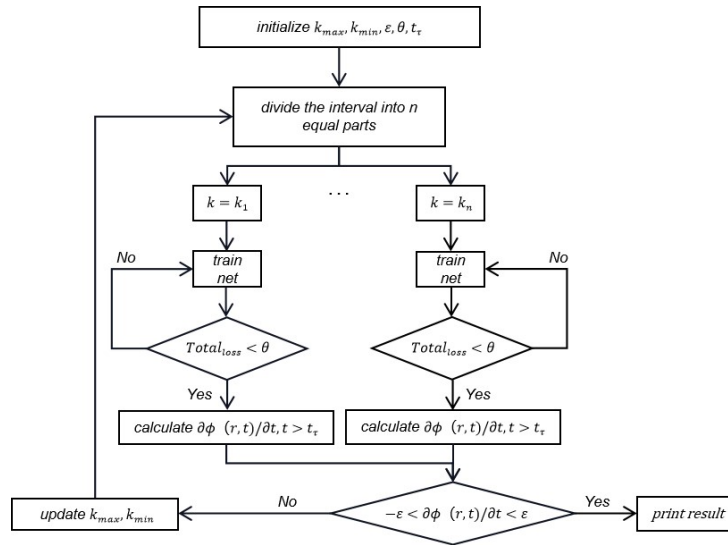
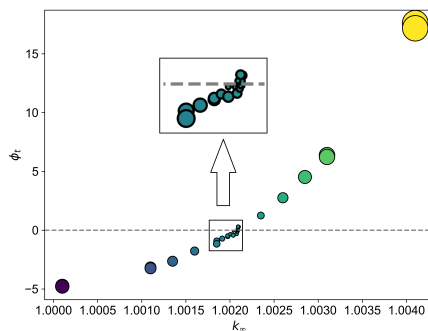
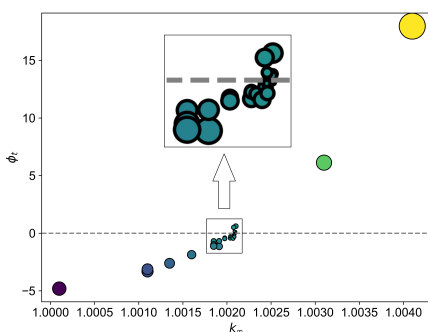


Fig. 14. Search Flowchart[28].

(a) $\phi_0 = \phi_1$ (b) $\phi_0 = \phi_2$ Fig. 15. Search Result of ϕ_t .

So, during the training section, at regular intervals, check if the rate of change of fluxes converges. When ϕ_t is converged, stop the training section and soon begin the next k -value network training. This will result in a faster parameter search without loss of accuracy. The equation for determining when

to stop the network iterating is shown below:

$$\frac{((\phi_t)_{i+1} - (\phi_t)_i)}{((\phi_t)_i - (\phi_t)_{i-1})} < \lambda \quad (27)$$

The parameter λ is set to 0.01, and every 200 iterations, compute the Eq. 27 to determine whether the network stops iterating. After using it, the comparative result when $\phi_0 = \phi_1$ is shown in Table 10. The early termination mechanism can significantly reduce the search time, which is just 0.56 times the original one.

Table 10. Time Consume Comparison.

	Cost Time	Search Result
FCN	7841s	1.00202
R ² -PINN	1837s	1.00208
R ² -PINN(Early Termination)	1027s	1.00207

On the other hand, according to Fig. 15, it can be seen that ϕ_t is exponentially related to k . Therefore, it can be used to find the critical corresponding value of k by fitting the quadratic function. To optimize search algorithms, the experiment was conducted to compare three search methods: binary search method, grid search method, and quadratic fitting search method. Using R²-PINN with an early termination mechanism, the results are shown in the following in Fig. 17.

The quadratic fitting search method quickly finds the k_{eff} in 250s and reaches e-04 accuracy, while the grid search method can find the k_{eff} in 522s and reach e-05 accuracy. Different methods can be chosen for parameter search based on the actual need for time and accuracy.

F. Network Prediction for Different k : R²-PINN's Robustness

The network is trained at different k_∞ values and compared results with the analytical solution generated to obtain the ac-

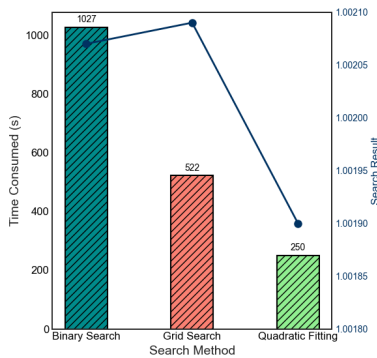
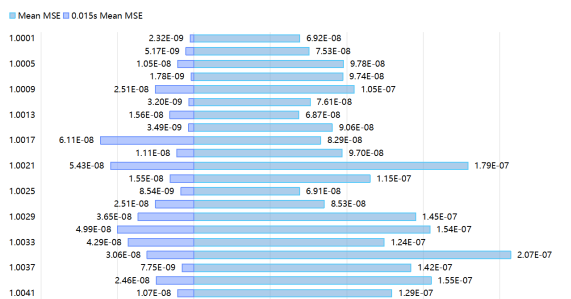


Fig. 17. Comparison of Search Method.

Table 11. MSE Results in Different k_{∞} .

k_{∞}	MSE	t=1s MSE
1.1	4.4e-6	9.0e-6
1.11	1.1e-6	1.7e-6
1.12	3.2e-6	5.2e-6
1.13	1.2e-6	2.2e-6
1.14	1.8e-6	3.0e-6
1.15	8.5e-7	1.6e-6
1.16	2.4e-6	4.4e-6
1.17	1.1e-5	2.2e-5
1.18	5.5e-6	9.3e-6
1.19	2.2e-6	4.7e-6
1.2	4.5e-6	8.2e-6

curacy at each k_{∞} value, as shown in Fig. 18, to validate the robustness of R²-PINN.

Fig. 18. MSE Accuracy Comparison in Different k_{∞} .

The robustness of the R²-PINN network is evident from Fig. 18. Across all tested values, the network consistently maintains a high accuracy of e-7 or higher, indicating its ability to handle various scenarios and maintain reliable predictions. The observed differences in MSE across different parameter values are relatively small, further highlighting the network's stability and effectiveness. The robustness of the R²-PINN network is evident from its consistently high accuracy across different parameter values.

G. R²-PINN for solving a Two-dimensional reactor diffusion equation for a single energy group

In this experiment, an 11-layer S-CNN network is used for training, and the rest of the hyperparameters are chosen as in Section IV D.

To validate the generalizability of models, the experiment is conducted between different k_{∞} , and the results are shown in Table 11, where the network achieves e-5 accuracy under different parameters, and the MSE for the extrapolation region, i.e., the t = 1 region, still achieves e-5 accuracy, which proves that the model performs well in temporal extrapolation ability and can be used to search for the parameters corresponding to the critical state.

Searching for the k_{∞} parameter in the same way as in Section IV D yields $k_{eff} = 1.1378$. While using the source iteration method find $k_{\infty} = 1.1202$. The calculation error is around 1.6%. The results of the prediction and the reference truth are shown in Fig. 19. The error plot is shown in Fig. 20.

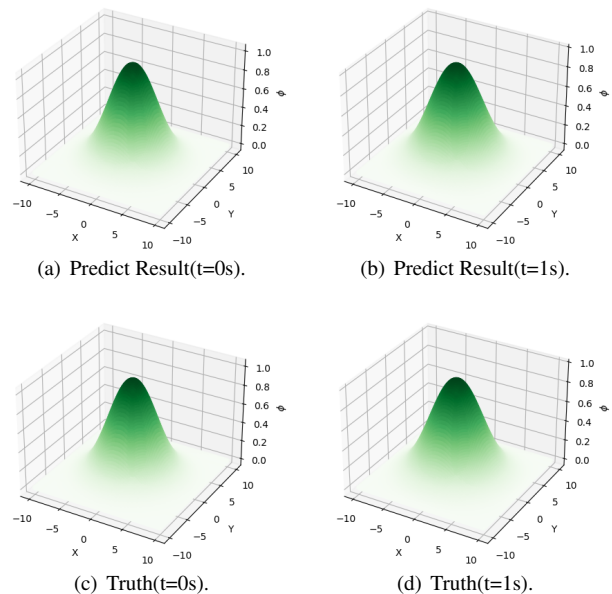


Fig. 19. Comparison Between Result and Truth.

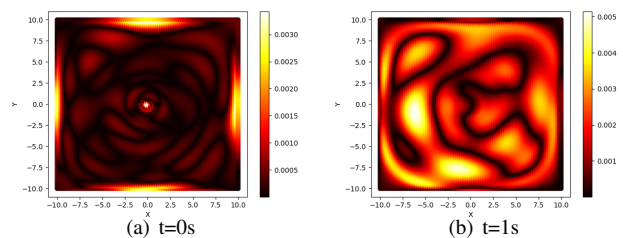


Fig. 20. Loss Field.

H. R²-PINN for solving Two-dimensional rectangular geometry multigroup multi-material diffusion problem

In this two-group problem, we separately predict the neutron flux of the fast group (ϕ_1) and the thermal group (ϕ_2) using dual PINNs at ($k_{eff} = 0.9693$). As there is an inter-conversion relationship between the fluxes, the dual PINNs share losses and undergo sequential iterative optimization. The experiment utilizes a 4-layer S-CNN for training. Other PINN parameters remain consistent with those in Section IV D. Using R²-PINN, MSE of ϕ_1 reaches 1.36e-06, MSE of ϕ_2 reaches 2.49e-07. The results and reference solutions are shown in Fig. 21, Fig. 22.

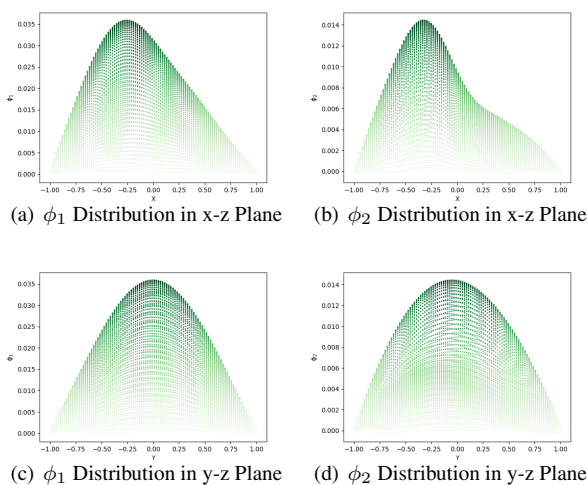


Fig. 21. Predict Result.

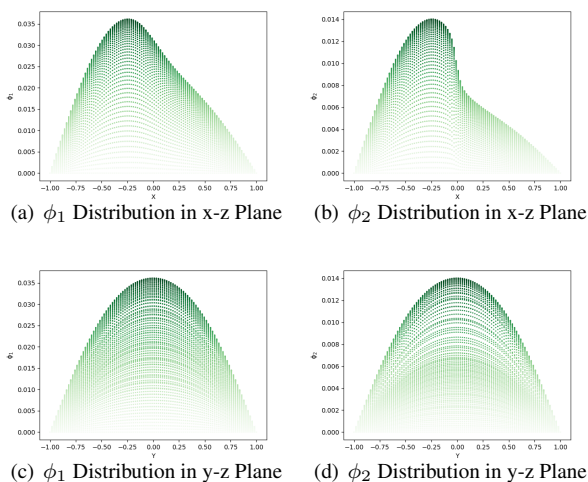


Fig. 22. Truth Result.

Due to the small value of the flux, to make the error representation clearer, we also calculated the loss rate and displayed it in Fig. 23. Specific equations are shown in Eq. 28.

$$loss\ rate = ABS(\phi_{predict} - \phi_{truth})/\phi_{truth} \quad (28)$$

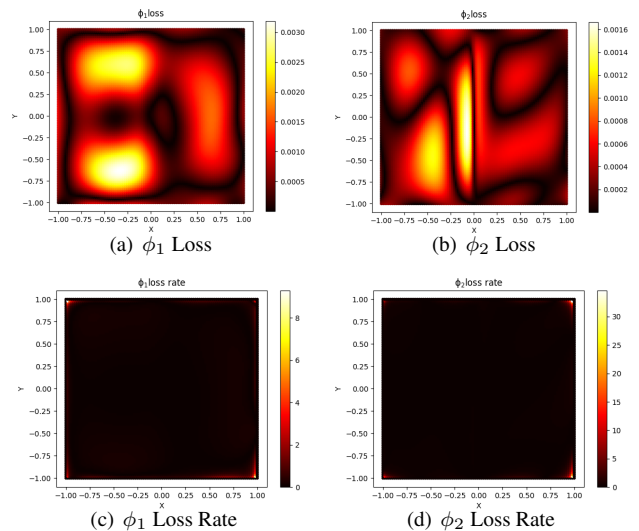


Fig. 23. Loss Field and Loss Rate Field.

The results show that we can effectively find the steady-state flux distribution under the specified k_{eff} according to the steady-state equations, and at the same time, according to the experiments in Section IV D and Section IV G, we are also able to find the critical parameters according to the transient equations, so the model can be well adapted to and solved the two major problems of nuclear reactors, i.e., solving for the steady-state fluxes as well as solving for the steady-state parameters.

I. R²-PINN for solving 2D-IAEA problem

Using a 6-layer R²-PINN structure, incorporates k_{eff} as a parameter for iterative optimization in the neural network training. The model utilized 18000 points for compute $Loss_{PDE}$, 500 points for $Loss_{Boundary}$ and 76 points for $Loss_{data}$.

Ultimately, relative error and relative L_∞ error are used to evaluate the accuracy of R²-PINN, with relative L_∞ error being particularly important in the nuclear engineering domain. The specific equations are shown in Eq. 29 and Eq. 30. The prediction results and the reference truth are presented in Fig. 24. Additionally, the absolute error plot is depicted in Fig. 25.

$$e_r = ABS(\phi_{predict} - \phi_{truth})/\phi_{truth} \quad (29)$$

$$e_\infty = \frac{\|\phi_{predict} - \phi_{truth}\|_\infty}{\|\phi_{truth}\|_\infty} \quad (30)$$

Table 12. Results of 2D-IAEA benchmark.

k_{eff}	e_r of k_{eff}	e_∞ of ϕ_1	e_∞ of ϕ_2
1.02977	1.797e-4	0.008	0.038

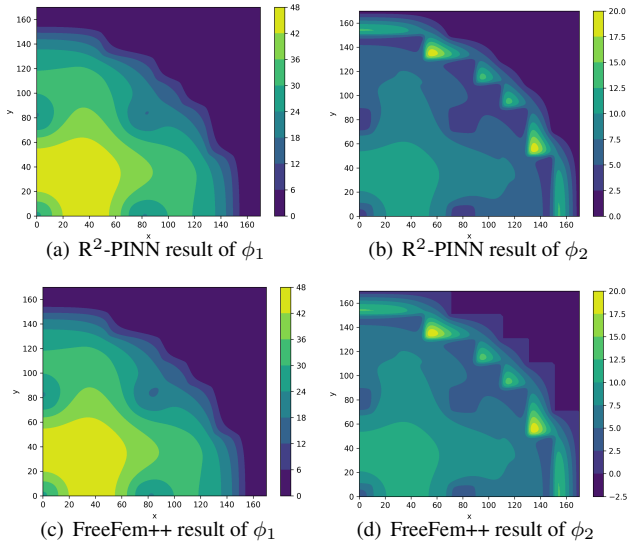


Fig. 24. Comparison Between Results and Reference.

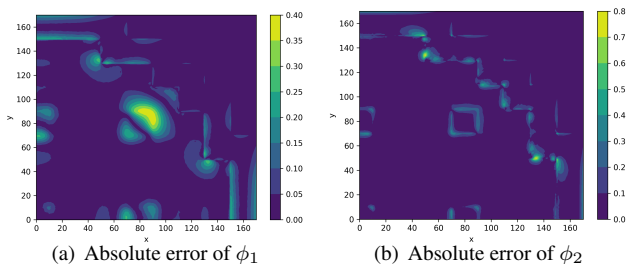


Fig. 25. Absolute Loss Field.

Considering the engineering acceptance criteria for the 2D IBP, the flux calculation error in fuel assemblies with a relative flux higher than 0.9 must be less than 5%, and in fuel assemblies with a relative flux less than 0.9, the flux calculation error must be less than 8%. Additionally, the relative error of k_{eff} must be less than 0.005 [46]. The predicted results meet these acceptance criteria, indicating that R²-PINN also has practical engineering application value.

V. RESULTS AND DISCUSSION

The ablation study on the number of layers revealed that increasing the depth of the S-CNN architecture improved accuracy. Notably, a kernel size of 1 yielded superior results. However, there was an accuracy bottleneck, making overly deep layers unnecessary. In Section IV B, S-CNN outperformed the FCN architecture across various layer configurations. Even when the number of layers was doubled, vanish-

ing gradients did not occur. Adding skip connections effectively mitigated vanishing gradients, enhancing the model's stability, robustness, and overall accuracy.

Meanwhile, in Section IV C, the sensitivity analysis of the resample parameter revealed that the optimal R²-PINN configuration is a resample granularity of 2 and 500 resamples. Setting the loss weight coefficient w to 100 achieved the best prediction performance, resulting in lower other losses compared to the PDE loss. The test loss in Fig. ?? shows a smooth training process without significant fluctuations. Around 2000 epochs, the LBFGS optimizer automatically stops training, achieving an MSE accuracy of e-07, indicating high precision.

Further, k_{eff} is found by searching the critic state in Section IV D using the adjusted R²-PINN. R²-PINN quickly converged in just 1000 epochs and reached the e-08 accuracy. The fast convergence speed and high convergence accuracy of the model suggest that the model is suitable for parameter search goals that require the training of multiple networks.

Then, multiple search methods are compared in Section IV E to improve the search efficiency. From the experiment result, the quadratic fitting search method can quickly find the k_{eff} only in two k -value search processes, with e-04 accuracy in just 250s. This shows the great value in the scenarios with high real-time requirements. Meanwhile, the grid method can also achieve the parameter search with e-05 accuracy within 10 minutes. When high accuracy is required, the grid method can set the optimal grid refine numbers to reach an acceptable duration with higher accuracy.

By conducting experiments in different k in Section IV F, the result shows that our R²-PINN network has exceptional performance in capturing the system's dynamics within the domain Ω_1 . This region exhibits a significant improvement in accuracy compared to FCN networks. By accurately representing this specific region's intricate features and sharp gradients, our network enables more precise determinations of whether the system is in a steady state. This enhanced accuracy proves invaluable when conducting parameter searches, allowing for higher precision and more reliable results.

Finally, to verify the generalizability of the model, the experiments were computed using the S-CNN architecture for 2D single-cluster in Section IV G and the parameter search error is around 1.6%. Using S-CNN solving 2D multi-cluster multi-material in Section IV H gives the solution with e-06 accuracy. Standardized test problem sets—2D-IAEA benchmark for search k_{eff} reach e-4 accuracy in Section IV I. These result shows the model can effectively predict the variation of physical quantities in the physical field under multiple equations, different initial conditions, and boundaries and has good generalization under different scenarios.

In summary, the R²-PINN network performs better than FCN networks in solving neutron diffusion equations. The accuracy improvement of 1-2 points is noteworthy, considering the computational efficiency achieved by our framework. This efficiency reduces the computational burden and maintains high accuracy, making it a promising approach for practical applications. By using a suitable search method, our architecture has good real-time performance.

VI. CONCLUSIONS

This paper introduces a novel and innovative framework called R^2 -PINN that addresses the persistent challenge of the disappearing gradient phenomenon in DNN. Additionally, our framework is designed to enhance the accuracy and computational efficiency of PINNs when solving neutron diffusion equations. R^2 -PINN can find k_{eff} with e-04 accuracy in just 250s. The single NN accuracy reached e-08 accuracy on average, which is an order of magnitude higher than FCN. The S-CNN architecture is integrated into the R^2 -PINN framework to overcome the vanishing gradients. By leveraging cross-layer connections, our model effectively learns residual information, thereby improving the depth and expressive power of the network. This architectural enhancement ensures that the network can effectively propagate gradients through the layers, enabling more accurate and stable learning. Furthermore, the RAR method is introduced to enhance the representation and sampling strategy within the network. The RAR method allows for the adaptive collection of sample points, ensuring that the model captures essential features and gradients in the solution space. This refinement strategy dramatically improves the network's capacity to handle sharp gradients and intricate features in PDE solutions.

In the experimental section, comprehensive comparative experiments were conducted to optimize our R^2 -PINN framework. Through meticulous parameter tuning, including adjusting the number of layers, kernel size, and resampling hy-

perparameters, R^2 -PINN achieved significant accuracy improvements of 1-2 units compared to FCN, demonstrating its effectiveness in enhancing PDE solutions. The parameter search capability of R^2 -PINN was validated by efficiently determining the corresponding value of k when it enters the critical state within the specified search interval through high-precision network predictions. To evaluate model robustness and accuracy under varying parameters, MSE validation experiments with different values of k were conducted, consistently yielding high accuracy results. Finally, for complex models like the two-dimensional single-group neutron diffusion equation, two-group two-material neutron diffusion equation models, and 2D-IAEA benchmark, the search for effective value-added coefficients and the steady-state flux distribution solution was successfully carried out.

Overall, the experimental results confirm that the integration of S-CNN and the RAR mechanism in R^2 -PINN empowers the network to capture intricate features and sharp gradients in PDE solutions. The adaptive refinement strategy significantly improves the distribution of residual points, enhancing the network's ability to represent complex physical systems accurately. Our findings provide compelling evidence of the potential of R^2 -PINN to advance the field of deep learning-based PDE solving. Not only does our framework outperform existing methods, but it also exhibits promising potential for application in real-world physical systems. The contributions of our work hold substantial implications for the development of more accurate and efficient models in various science and engineering domains.

-
- [1] Xie, ZS., *Physical Analysis of Nuclear Reactors*. (Xi'an Jiaotong University Press, Xi'an, 2004), pp. 49-74. (in Chinese)
 - [2] M. N. Özişik, H. R. Orlande, M. J. Colaço et al., *Finite difference methods in heat transfer*, 2nd edn. (CRC press, Inc, 2017)
 - [3] A. Younes, P. Ackerer, F. Delay, Mixed finite elements for solving 2-d diffusion-type equations. *Rev. Geophys.* **48**, 1(2010). <https://doi.org/10.1029/2008RG000277>
 - [4] Y.M. Hamada, Higher order compact finite difference schemes for steady and transient solutions of space-time neutron diffusion model. *Ann. Nucl. Energy.* **175**, 109177(2022). <https://doi.org/10.1016/j.anucene.2022.109177>
 - [5] S. Yuk, J. Cho, C. Jo et al., Time-dependent neutron diffusion analysis using finite element method for a block-type vhr core design. *Nucl. Eng. Des.* **360**, 110512(2020). <https://doi.org/10.1016/j.nucengdes.2020.110512>
 - [6] Li, XY., Kun, C., Tao H. et al., Research on neutron diffusion equation and nuclear thermal coupling method based on gradient updating finite volume method. *Ann. Nucl. Energy.* **195**, 110158(2024). <https://doi.org/10.1016/j.anucene.2023.110158>
 - [7] M. G. Tavares, C. Z. Petersen, M. Schramm et al., Solution for the multigroup neutron space kinetics equations by source iterative method. *Braz. J. Radiat. Sci.* **9**(2A), Suppl(2021). <https://doi.org/10.15392/bjrs.v9i2A.731>
 - [8] Zhuang K., Shang W., Li T. et al., Variational nodal method for three-dimensional multigroup neutron diffusion equation based on arbitrary triangular prism. *Ann. Nucl. Energy.* **158**, 108285(2021). <https://doi.org/10.1016/j.anucene.2021.108285>
 - [9] Huang Z., Yuan Y., Liu GM. et al., Solution of Neutron Diffusion Problem Based on COMSOL Multiphysics and Its Application Analysis on Micro Gas-cooled Reactor. *Atomic Energy Sci. Technol.* **57**, 565-575(2023). <https://doi.org/10.7538/yzk.2022.youxian.0354>. (in Chinese)
 - [10] K. Sidi-Ali, E.M. Medouri, D. Ailem et al., Neutronic calculations and thermalhydraulic application using CFD for the nuclear research reactor NUR at steady state mode. *Prog. Nucl. Energy.* **159**, 104640(2023). <https://doi.org/10.1016/j.pnucene.2023.104640>
 - [11] Ma Y., Wang YH., Yang JH., ntkFoam: An OpenFOAM based neutron transport kinetics solver for nuclear reactor simulation. *Comput. Math. Appl.* **81**, 512-531(2021). <https://doi.org/10.1016/j.camwa.2019.09.015>
 - [12] Karniadakis, G.E., Kevrekidis, I.G., Lu, L. et al., Physics-informed machine learning. *Nat Rev Phys.* **3**, 422-440(2021). <https://doi.org/10.1038/s42254-021-00314-5>
 - [13] Cuomo, S., Di Cola, V.S., Giampaolo, F. et al., Scientific Machine Learning Through Physics-Informed Neural Networks: Where we are and What's Next. *J Sci Comput.* **92**, 88(2022). <https://doi.org/10.1007/s10915-022-01939-z>
 - [14] M. Raissi, P. Perdikaris, G.E. Karniadakis, Physics-informed neural networks: A deep learning framework for solving forward and inverse problems involving nonlinear partial differential equations. *J. Comput.* **378**, 686-707(2019). <https://doi.org/10.1016/j.jcp.2018.10.045>
 - [15] Cai SZ., Mao ZP., Wang ZC. et al., Physics-informed neural networks (PINNs) for fluid mechanics: a review. *Acta Mech. Sin.* **37**, 1727-1738(2021). <https://doi.org/10.1007/s10409->

- 021-01148-1
- [16] Xu BC., Zhang XZ., Wang YX. et al., Self-adaptive physical information neural network model for prediction of two-phase flow annulus pressure. *Acta Petrol. Sin.* **44**, 545(2023). <https://doi.org/10.7623/syxb202303012>. (in Chinese)
- [17] Cai SZ., Wang ZC., Wang SF. et al., Physics-Informed Neural Networks for Heat Transfer Problems. *J. Heat Transfer.* **143**(6), 060801(2021). <https://doi.org/10.1115/1.4050542>
- [18] Yu B., Gan ZY., Zhang SL. et al., PREDICTION OF 2D/3D UNSTEADY-STATE TEMPERATURE FIELDS AND HEAT SOURCES UPON THE PHYSICS-INFORMED NEURAL NETWORKS. *Engineering Mechanics.* **41**, 1-13(2023). <https://doi.org/10.6052/j.issn.1000-4750.2023.04.0282>. (in Chinese)
- [19] Mao ZP., A.D. Jagtap, G.E. Karniadakis, Physics-informed neural networks for high-speed flows. *Comput Methods Appl Mech Eng.* **360**, 112789(2020). <https://doi.org/10.1016/j.cma.2019.112789>
- [20] Chen C., Zhang GT., Deep learning method based on physics informed neural network with resnet block for solving fluid flow problems. *Water.* **13**(4), 423(2021). <https://doi.org/10.3390/w13040423>
- [21] Bai JS., Rabczuk T., Gupta A. et al., A physics-informed neural network technique based on a modified loss function for computational 2d and 3d solid mechanics. *Comput Mech.* **71**, 543-562(2023). <https://doi.org/10.1007/s00466-022-02252-0>
- [22] Feng TSJ., Liang W., The buckling analysis of thin-walled structures based on physics-informed neural networks. *Acta Mech. Sin.* **55**(11), 2539-2553(2023). <https://doi.org/10.6052/0459-1879-23-277>. (in Chinese)
- [23] Liu P., Shi DF., Li R. et al., Simulation of Core Physics Benchmark VERA Based on Monte Carlo Code JMCT. *Atomic Energy Sci. Technol.* (in Chinese) **57**, 1131-1139(2023). <https://doi.org/10.7538/yzk.2022.youxian.0593> (in Chinese)
- [24] Guo H., Wu YW., Song QF. et al. Development of multi-group Monte-Carlo transport and depletion coupling calculation method and verification with metal-fueled fast reactor. *NUCL SCI TECH* **34**, 163 (2023). <https://doi.org/10.1007/s41365-023-01310-3>
- [25] Daher, D.H., Kotb, M., Khalaf, A.M. et al. Simulation of a molten salt fast reactor using the COMSOL Multiphysics software. *NUCL SCI TECH* **31**, 115 (2020). <https://doi.org/10.1007/s41365-020-00833-3>
- [26] Yang QH., Yang Y., Deng YT. et al., Physics-constrained neural network for solving discontinuous interface K-eigenvalue problem with application to reactor physics. *NUCL SCI TECH* **34**, 161 (2023). <https://doi.org/10.1007/s41365-023-01313-0>
- [27] Hao YS., Wu Z., Pu YH. et al., Research on inversion method for complex source-term distributions based on deep neural networks. *NUCL SCI TECH* **34**, 195 (2023). <https://doi.org/10.1007/s41365-023-01327-8>
- [28] Liu D., Luo Q., Tang L. et al., Solving multi-dimensional neutron diffusion equation using deep machine learning technology based on pinn model. *Nuclear Power Engineering.* **43**(2), 1-8(2022). <https://doi.org/10.13832/j.jnpe.2022.02.0001>. (in Chinese)
- [29] Liu D., Tang L., An P. et al., The Deep Learning Method to Search Effective Multiplication Factor of Nuclear Reactor Directly. *Nuclear Power Engineering.* **44**(5), 6-14(2023). <https://doi.org/10.13832/j.jnpe.2023.05.0006> (in Chinese)
- [30] Shen C., Yan L. Recent development of hydrodynamic modeling in heavy-ion collisions. *NUCL SCI TECH* **31**, 122 (2020). <https://doi.org/10.1007/s41365-020-00829-z>
- [31] Lu L., Meng XH., Mao ZP. et al., Deepxde: A deep learning library for solving differential equations. *SIAM REV.* **63**(1), 208-228(2021). <https://doi.org/10.1137/19M1274067>
- [32] L. D. McClenny, U. M. Braga-Neto, Self-adaptive physics-informed neural networks. *J. Comput.* **474**, 111722(2023). <https://doi.org/10.1016/j.jcp.2022.111722>
- [33] Wang Z., Xia H., Zhu S. et al., Cross-domain fault diagnosis of rotating machinery in nuclear power plant based on improved domain adaptation method. *NUCL SCI TECH.* **59**(1), 67-77(2022). <https://doi.org/10.1080/00223131.2021.1953630>
- [34] Z. K. Lawal, H. Yassin, D. T. C. Lai et al., Physics-informed neural network (pinn) evolution and beyond: a systematic literature review and bibliometric analysis. *Big Data Cogn. Comput.* **6**(4),140(2022). <https://doi.org/10.3390/bdcc6040140>
- [35] Fang ZW., A high-efficient hybrid physics-informed neural networks based on convolutional neural network. *IEEE Trans Neural Netw Learn Syst.* **33**(10),5514-5526(2021). <https://doi.org/10.1109/TNNLS.2021.3070878>
- [36] Yang XY., Zhou ZX., Li LH. et al., Collaborative robot dynamics with physical human-robot interaction and parameter identification with PINN. *Mech Mach Theory.* **189**, 105439(2023). <https://doi.org/10.1016/j.mechmachtheory.2023.105439>
- [37] Wu CX., Zhu M., Tan QY. et al., A comprehensive study of non-adaptive and residual-based adaptive sampling for physics-informed neural networks. *Comput Methods Appl Mech Eng.* **403**, 115671(2023). <https://doi.org/10.1016/j.cma.2022.115671>
- [38] McKay, M.D., Beckman, R.J. et al., A Comparison of Three Methods for Selecting Values of Input Variables in the Analysis of Output from a Computer Code (JSTOR Abstract). *Technometrics.* **21**(2), 239-245(1979). <https://doi.org/10.2307/1268522>
- [39] Liu M., Chen LM., Du XH. et al., Activated Gradients for Deep Neural Networks. *IEEE Trans Neural Netw Learn Syst.* **34**(4), 2156-2168(2023). <https://doi.org/10.1109/TNNLS.2021.3106044>
- [40] Stacey M.W., *Nuclear Reactor Physics*, 2nd edn. (Wiley, Weinheim, 2010), pp. 43-60
- [41] Duderstadt JJ, *Nuclear Reactor Analysis*. (Wiley, New York, 1976), pp. 74-88
- [42] None N, *Argonne Code Center: Benchmark problem book*. (Argonne National Lab.(ANL), Argonne, 1977), pp.277-284
- [43] He KM., Zhang XY., Ren SQ. et al., Deep residual learning for image recognition. 2016 IEEE Conference on Computer Vision and Pattern Recognition(CVPR). Las Vegas, USA 2016, pp. 770-778 (2016). <https://doi.org/10.1109/CVPR.2016.90>
- [44] Hecht, F., New development in FreeFem++. *J. Numer. Math.* **20**(3-4), 251-265(2012). <https://doi.org/10.1515/jnum-2012-0013>
- [45] Lehoucq, R.B., Sorensen, D.C., Yang, C., *ARPACK Users' Guide: Solution of Large-Scale Eigenvalue Problems with Implicitly Restarted Arnoldi Methods*. (SIAM, 1998), pp. 21-40 <https://doi.org/10.1137/1.9780898719628>
- [46] Yang Y, Gong H, Zhang S, et al., A data-enabled physics-informed neural network with comprehensive numerical study on solving neutron diffusion eigenvalue problems. *Ann. Nucl. Energy.* **183**, 109656(2023). <https://doi.org/10.1016/j.anucene.2022.109656>